Numerical simulation of lowering operations from the coupling between the Composite-Rigid-Body Algorithm and the weak-scatterer approach

Pierre-Yves Wuillaume, Aurélien Babarit, François Rongère, Mattias Lynch, Pierre Ferrant

Version of Record: https://www.sciencedirect.com/science/article/pii/S0029801821013342
Manuscript_f1d17c053352fd4324020e6831bbaea0

Numerical simulation of lowering operations from the coupling between the Composite-Rigid-Body Algorithm and the weak-scatterer approach

Pierre-Yves Wuillaume[a,b,*], Aurélien Babarit[b], Francois Rongère[b,**], Mattias Lynch[a] and Pierre Ferrant[a]

[a] *INNOSEA, 1 Rue de la Noe, 44321 Nantes, France*
[b] *Ecole Centrale de Nantes, LHEEA lab. (CNRS), 1 Rue de la Noe, 44300 Nantes, France*

ARTICLE INFO

Keywords:
Marine operation
Multibody dynamics
Potential flow theory
Weak-scatterer
Wave-structure interaction

ABSTRACT

A consistent frame for the numerical simulation of lowering operations is investigated in this paper from a new wave-structure coupling. The mechanical modeling is based on the Compostite-Rigid-Body Algorithm, which is able to simulate the nonlinear dynamics of multibody systems. The hydrodynamic model is based on the weak-scatterer approach, which allows the computation of unsteady hydrodynamic loads without being limited by the classical hypotheses of the linear potential flow theory. The coupling of these two models leads to the numerical simulation of articulated multibody systems with large relative motion in waves. The coupling equation is derived in this paper.

This new numerical modeling is compared to the classical linear potential flow theory in the case of a lowering operation with a payload in the water. The impact of the lowering velocity is studied. Results show that this new model matches the classical approach for small lowering velocities but as soon as nonlinearities arise, differences between the two models appear.

1. Introduction

A floating crane vessel is a crane-mounted ship used to lift or lower heavy payloads. They are widely used in marine operations, for instance in shipyard or for transportation, installation or retrieval of offshore marine structures or for loading arm operations between side-by-side offloading vessels. The development of marine renewable energies leads to an increase of these installation operations for wind turbine farms Figure 1a or tidal turbines Figure 1b for example. To schedule these operations, establish the operational conditions (weather windows), design the equipments or predict the body motions to reduce risks, collisions or any injury to the workers, numerical simulation has become an essential tool.

The numerical simulation of lowering or lifting operations at sea has been extensively studied in the literature. These works can be gathered in three domains: structural analysis, hydrodynamic analysis and motion control analysis (not considered here).

Offshore lowering or lifting operations require to model an articulated multibody system. The first structural studies were based on simplified approaches. For instance, by assumption, the crane tip follows a prescribed motion. This mechanical model uncouples the dynamics of the payload from the dynamics of the floating crane. It assumes that the payload does not influence the crane and the supporting vessel. Elling and McClinton (1973) and Chin et al. (2001) computed the dynamics of a single concentrated mass, such as a pendulum, linked to a crane tip by a rigid cable with a prescribed harmonic displacement of the boom. This approach allows studying the motion of the payload subject to a parametric excitation. It is also possible to linearize the motion equation at the system's equilibrium position. The purpose of a linearized model is to perform a frequency-domain analysis and compute the natural frequencies of the system (Schellin et al., 1991, 1993). Another simplification is to consider a two-dimensional problem. Ellermann et al. (2002) and Ellermann and Kreuzer (2003) simulated a floating crane linked to a suspended lumped mass by assuming a motion in a vertical plane.

Uncoupled or linearized or two-dimensional models suffer from a lack of generality. Payload dynamics may influence the motion of the floating crane in case of heavy lifting operations, nonlinearities are present in the physics (mechanics, mooring, hoisting cable dynamics, etc.) and a two-dimensional model restricts the simulation to planar motions. Thus, more complex coupled models are necessary.

Many studies (Van Den Boom et al. (1988); Schellin et al. (1993); Witz (1995); Malenica et al. (2005), etc.) were devoted to the simulation of a floating crane with a payload hanging in the air. The problem is in three dimensions and the cable is either rigid or elastic. Only few studies consider the payload in the water. The dynamics of a submerged payload with a constrained motion using a rigid cable was studied by Bai et al. (2014). Hannan and Bai (2016) performed

*Corresponding author, now at D-ICE Engineering (pierre-yves.wuillaume@dice-engineering.com)
**Now at D-ICE Engineering (francois.rongere@dice-engineering.com)
pierre-yves.wuillaume@ec-nantes.fr (P. Wuillaume); aurelien.babarit@ec-nantes.fr (A. Babarit); francois.rongere@ec-nantes.fr (F. Rongère); mattias.lynch@innosea.fr (M. Lynch); pierre.ferrant@ec-nantes.fr (P. Ferrant)
ORCID(s):
[1] http://www.scaldis-smc.com
[2] https://www.sabella.bzh

(a) Transportation of a wind turbine[1]

(b) Lifting of a tidal turbine[2]

Figure 1: Installation operations

a dynamical analysis of the same constrained payload near a floating barge. The barge was motionless, which simplified the mechanical problem. They used phase trajectories, Poincaré maps and bifurcation diagrams to analyse the payload motion in waves.

Since Cha et al. (2010), mechanical models have started being based on fully coupled multibody dynamics. These authors used constraint equations to include the internal degrees of freedom of their multibody system. Using this approach, they could simulate two rigid bodies with six degrees of freedom each and linked by an elastic cable (a floating crane with a lifted heavy cargo). This model was also used by Ku and Roh (2015) in order to simulate the dynamic response of an offshore wind turbine suspended in the air by a floating crane.

So far, motion equations were derived specifically for each multibody system. In case of a change in the multibody system, they had to be derived again. Hence, it became convenient to use multibody dynamic algorithms to write automatically the motion equations for most or any multibody systems. Three families of multibody systems may be established: open-loop or open-chain system Figure 2a, kinematic trees or open-chain with multiple branches Figure 2b and closed-loop systems Figure 2c. Open-loop systems are unbranched kinematic trees and are composed of bodies which have exactly one ancestor and one successor. With kinematic trees, each body may have several successors but always a single ancestor. Closed-loop systems form the most general case. Each body may have several successors and ancestors, leading to kinematic loops. Ku and Ha (2014) used multibody dynamic algorithms based on the Newton-Euler equation to model a heavy load lifting operation with multicranes. These algorithms are based on a recursive formulation and can be applied to all types of multibody systems. Ham et al. (2015) preferred the Euler-Lagrange equation. They formulated it with constraint equations. An application was done with a dynamic analysis of a floating crane with two booms and a heavy load in the air.

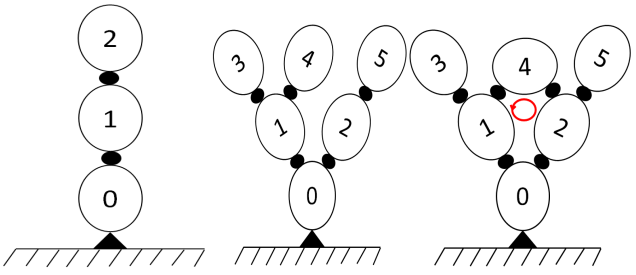

(a) Open-loop system **(b)** Kinematic tree **(c)** Closed-loop system

Figure 2: Sketches of the different multibody system families. Black circle: body, black point: joint and red arrow: kinematic loop.

Regarding the hydrodynamic analysis of lowering and lifting operations, most of the studies were based on the linear frequency-domain potential flow theory (Van Den Boom et al., 1988; Schellin et al., 1993; Malenica et al., 2005; Cha et al., 2010; Ku and Roh, 2015). A linear time-domain potential flow theory was used by Ku and Ha (2014). The linear theory (both in frequency and time domains) assumes a small amplitude motion of the bodies and a small steepness of the waves. The frequency domain also involves the steadiness of the body motions. It is valid when the payload is in the air as it is the case in the majority of the works. When the payload is in the water and is lowered or lifted, the linear potential flow theory is not applicable with consistency. The presence of two bodies close to each other leads to hydrodynamic interactions and the lowering or the lifting of the payload may involve a large relative amplitude motion.

That is why, Hannan (2014) used a fully nonlinear po-

tential flow theory to simulate such marine operations in his PhD work. In this case, the assumptions of the linear theory do not have to be satisfied. One part of his work focused on the motion of a fully immersed cylinder in waves and subject to a constrained pendulum motion with a lowering velocity (Bai et al., 2014). He also studied the hydrodynamic interactions between a fixed floating barge and the same cylindrical payload (Hannan and Bai, 2016). The presence of the barge close to the payload modified the motion of this latter due to the hydrodynamic interactions. As the floating crane was fixed, there was no mechanical interaction but only hydrodynamic interactions. A fully nonlinear potential flow based solver, although more accurate than a linear potential flow based solver, has limitations and may present numerical challenges. Moreover, the CPU time is much greater compared to the linear approach. The comparison between the nonlinear and linear potential flow theory in case of a lowering or lifting operation has never been achieved nor quantified in the literature. The interest of a nonlinear hydrodynamic stays an assumption yet.

If a payload is made of slender structures, it is possible to use the Morison's equation (Morison et al., 1950) to evaluate the hydrodynamic loads. This approach neglects the diffraction and the radiation damping and requires the knowledge of the necessary drag and added-mass coefficients. According to Li et al. (2015) in case of a monopile lowering, this method overpredicts the response of the bodies. Li et al. (2015) also developed a new approach based on the interpolation of the radiation loads at various depth of the payload, in order to assume steady-state conditions. The Morison's equation was used too. More accurate results were obtained than with the Morison's equation only. But this approach is limited to slender payloads in case of small lowering velocity to divide the lowering into stepwise steady-state conditions.

Wuillaume et al. (2017) used another hydrodynamic model to deal with lowering and lifting operation simulations: the weak-scatterer approach. It was introduced by Pawlowski and Bass (1991). This approach is based on the potential flow theory and the weak-scatterer hypothesis. It is assumed that the scattered wave components are much smaller than the incident wave components. Therefore large body motions, steep waves and unsteady hydrodynamic loads may be taken into account, contrary to the linear potential flow theory. Since 2012, a potential flow based solver, named *WS_CN* following the weak-scatterer hypothesis has been under development at LHEEA laboratory of Ecole Centrale de Nantes. The theory and the interest of the method were presented by Letournel et al. (2018) in the case of various submerged wave energy converters. *WS_CN* was extended to floating bodies by Chauvigné et al. (2015) and to multibody simulations by Wuillaume et al. (2018). It was shown in Wuillaume (2019) that the weak-scatterer hypothesis is fully relevant when the free surface nonlinearities and the body nonlinearities are important, which makes this approach consistent for being applied in case of a lowering or lifting operation.

WS_CN has been partially coupled by Wuillaume et al. (2017) with *InWave* (Combourieu et al., 2014) in view of simulating marine operations, leading to *InWaveS_CN*. *InWave* is a multibody solver which models kinematic trees (Figure 2b) and was developed by LHEEA laboratory of Ecole Centrale de Nantes and INNOSEA. The multibody dynamics algorithm of *InWave* is the Composite-Rigid-Body Algorithm. The solving of the wave-structure interaction was achieved in case of a single body subject to hydrodynamic loads and being the base of the multibody system (body numbered 0 in Figure 2). Thus, only a payload in the air could be considered.

The first objective of this study is the development of the coupling between the Composite-Rigid-Body Algorithm of *InWave* and the weak-scatterer approach of *WS_CN* in view of developing a numerical tool, *InWaveS_CN*, able to simulate with consistency a lowering operation with an immersed payload. The second objective is the comparison of such a modeling with the classical approach used in the litterature based on the linear potential flow theory.

The three first parts are dedicated to the presentation of the governing equations of the Composite-Rigid-Body Algorithm, the cable modeling and the weak-scatterer approach, respectively. Then, the coupling equation is derived in the fourth part. Finally, a comparison is made with the classical approach in the last part.

2. Governing multibody equations

The dynamics algorithm used through the numerical tool *InWave* is the Composite-Rigid-body Algorithm (*CRBA*). The *CRBA* simulates kinematic trees (Figure 2b) made of rigid bodies. By definition, the multibody system has $n+1$ bodies and each body has a number. The body numbered 0 is the base of the multibody system. Other bodies are numbered with increasing order from the base. Each body has a local frame Σ_j, of origin $\mathbf{O}_j$. The position of the center of gravity $\mathbf{G}_j$ of body j with respect to Σ_j is noted ${}^j\mathbf{S}_j$. The local base frame Σ_0 is defined with respect to the global earth-fixed inertial frame Σ_e, of origin $\mathbf{O}_e$. Only kinematic trees are considered, so each body j has a unique ancestor a_j. Only the base has no ancestor.

The base is also the unique body for which Cartesian coordinates with respect to Σ_e are used. Other bodies are located using the modified Denavit-Hartenberg parameters (*mDH*) (Khalil and Kleinfinger, 1986), which are a reduced set of coordinates to locate a body relatively to its unique ancestor. Their definition may be found in Rongère and Clément (2013). Only one-degree-of-freedom joints are considered, either revolute or prismatic. A revolute joint, respectively a prismatic joint, grants for a rotation, respectively a translation, between two bodies. The articular variable for the joint j is noted q_j. The parameter σ_j gives the nature of the joint j such as $\sigma_j = 0$ for revolute and 1 for prismatic. More complex joints may be produced using massless bodies to ensure the necessary degrees of freedom.

2.1. Kinematic recursive equations

To perform automatic dynamic computations, it is necessary to write the kinematic recursive equations between the bodies. To do so, several elementary quantities are defined and evaluated. From the modified Denavit-Hartenberg parameters, it is possible to compute (Rongère and Clément, 2013):

- ${}^{a_j}\mathbf{R}_j$: the rotation matrix from Σ_j to the ancestor local frame Σ_{a_j};
- ${}^{a_j}\mathbf{P}_j$: the position of the origin of Σ_j from the origin of Σ_{a_j} and expressed in Σ_{a_j}.

The six-component generalized position vector to locate Σ_j with respect to Σ_e in term of position and orientation is:

$$\boldsymbol{\eta}_j = \begin{pmatrix} \begin{pmatrix} x_j & y_j & z_j \end{pmatrix}^T \\ \begin{pmatrix} \varphi_j & \theta_j & \psi_j \end{pmatrix}^T \end{pmatrix} \tag{1}$$

with $x_j, y_j, z_j, \varphi_j, \theta_j$ and ψ_j the surge, sway, heave, roll, pitch and yaw of the body j, respectively. Cardan angles are used.

The six-component generalized velocity vector of body j with respect to Σ_e and expressed in Σ_j is:

$${}^j\mathbf{V}_j = \begin{pmatrix} {}^j\mathbf{v}_j \\ {}^j\boldsymbol{\omega}_j \end{pmatrix} \tag{2}$$

with:

- ${}^j\mathbf{v}_j$ the linear velocity of body j with respect to Σ_e at the point $\mathbf{O}_j$ and expressed in Σ_j.
- ${}^j\boldsymbol{\omega}_j$ the angular velocity of body j with respect to Σ_e and expressed in Σ_j.

The kinematic recursive equation for velocities is for the body j of unique ancestor $i = a_j$ (Rongère and Clément, 2013):

$${}^j\mathbf{V}_j = {}^j\mathbf{T}_i \, {}^i\mathbf{V}_i + \dot{q}_j \, {}^j\mathbf{a}_j \tag{3}$$

with:

- ${}^j\mathbf{T}_i$ the transformation matrix between the six-component generalized velocity vectors:

$${}^j\mathbf{T}_i = \begin{pmatrix} {}^j\mathbf{R}_i & -{}^j\mathbf{R}_i \mathbf{S}({}^i\mathbf{P}_j) \\ \mathbf{0}_{3\times3} & {}^j\mathbf{R}_i \end{pmatrix} \tag{4}$$

- $\mathbf{S}$ the skew-symmetric matrix of the cross product defined in Eq. (66);
- ${}^j\mathbf{a}_j$ the six-component generalized joint axis:

$${}^j\mathbf{a}_j = \begin{pmatrix} \sigma_j \, {}^j\mathbf{z}_j^T & \bar{\sigma}_j \, {}^j\mathbf{z}_j^T \end{pmatrix}^T \tag{5}$$

- ${}^j\mathbf{z}_j$ the joint axis of joint j in Σ_j:

$${}^j\mathbf{z}_j = \begin{pmatrix} 0 & 0 & 1 \end{pmatrix}^T \tag{6}$$

The kinematic recursive equation for accelerations is for the body j of unique ancestor $i = a_j$ (Rongère and Clément, 2013):

$${}^j\dot{\mathbf{V}}_j = {}^j\mathbf{T}_i \, {}^i\dot{\mathbf{V}}_i + {}^j\boldsymbol{\gamma}_j + \ddot{q}_j \, {}^j\mathbf{a}_j \tag{7}$$

with:

- ${}^j\dot{\mathbf{V}}_j$ the projection in Σ_j of the generalized acceleration vector of body j with respect to Σ_e:

$${}^j\dot{\mathbf{V}}_j = \begin{pmatrix} {}^j\dot{\mathbf{v}}_j \\ {}^j\dot{\boldsymbol{\omega}}_j \end{pmatrix} = \begin{pmatrix} {}^j\mathbf{R}_e \, {}^e\dot{\mathbf{v}}_j \\ {}^j\mathbf{R}_e \, {}^e\dot{\boldsymbol{\omega}}_j \end{pmatrix} \tag{8}$$

- ${}^j\boldsymbol{\gamma}_j$ the Coriolis and relative angular and linear accelerations:

$${}^j\boldsymbol{\gamma}_j = \begin{pmatrix} {}^j\mathbf{R}_i \mathbf{S}({}^i\boldsymbol{\omega}_i)\mathbf{S}({}^i\boldsymbol{\omega}_i) \, {}^i\mathbf{P}_j + 2\sigma_j \dot{q}_j \mathbf{S}({}^j\mathbf{R}_i \, {}^i\boldsymbol{\omega}_i) \, {}^j\mathbf{z}_j \\ (1-\sigma_j)\dot{q}_j \mathbf{S}({}^j\mathbf{R}_i \, {}^i\boldsymbol{\omega}_i) \, {}^j\mathbf{z}_j \end{pmatrix} \tag{9}$$

2.2. Multibody motion equation

The Composite-Rigid-Body Algorithm is based on the Newton-Euler equations. The multibody motion equation is:

$$\mathbf{H}_{MB}(\mathbf{q}) \begin{pmatrix} {}^0\dot{\mathbf{V}}_0 \\ \ddot{\mathbf{q}} \end{pmatrix} = \begin{pmatrix} \mathbf{0}_{6\times1} \\ \boldsymbol{\Gamma} \end{pmatrix} - \mathbf{C}(\mathbf{q}, \dot{\mathbf{q}}) \tag{10}$$

with:

- $\mathbf{H}_{MB} = \begin{pmatrix} \mathbf{H}_{11} & \mathbf{H}_{12} \\ \mathbf{H}_{21} & \mathbf{H}_{22} \end{pmatrix}$ the $(6+n)\times(6+n)$ generalized mass matrix of the multibody system;
- $\mathbf{H}_{11}$ the (6×6) mass matrix of the whole multibody system seen as a single rigid body;
- $\mathbf{H}_{22}$ the $(n \times n)$ mass matrix of the multibody system when the base is fixed;
- $\mathbf{H}_{12}$ the $(6 \times n)$ coupled mass matrix representing the inertial effects caused by the articulations on the base;
- $\mathbf{H}_{21} = \mathbf{H}_{12}^T$ the $(n \times 6)$ coupled mass matrix representing the inertial effects caused by the base on the articulations;
- $\mathbf{C} = \begin{pmatrix} \mathbf{C}_1 \\ \mathbf{C}_2 \end{pmatrix}$ the $(6 + n)$ vector of the external loads and the Coriolis and relative accelerations on the base ($\mathbf{C}_1$) and the articulations ($\mathbf{C}_2$). This vector depends neither on the base acceleration ${}^0\dot{\mathbf{V}}_0$ nor on the articular articulation $\ddot{\mathbf{q}}$.
- $\boldsymbol{\Gamma}$ the $(6 + n)$ vector of the internal loads along or around the joint axes;
- ${}^0\dot{\mathbf{V}}_0$ the acceleration of the base with respect to the global inertial frame and expressed in the base local frame;

- $\ddot{\mathbf{q}}$ the vector of the articular accelerations.

The solving of Eq. (10) requires the knowledge of $\mathbf{H}_{MB}$, $\mathbf{C}$ and $\mathbf{\Gamma}$. This latter is defined by the user of the multibody solver. The *CRBA* aims at computing $\mathbf{H}_{MB}$ and $\mathbf{C}$. It unfolds in three steps:

- a forward loop over the bodies in ascending order for evaluting the elementary kinematic quantities such as ${}^{i}\mathbf{R}_{j}$, ${}^{i}\mathbf{P}_{j}$, ${}^{i}\mathbf{T}_{j}$, ${}^{j}\mathbf{V}_{j}$ or ${}^{j}\boldsymbol{\gamma}_{j}$;
- a backward loop in descending order for computing the necessary projections of the mass matrices and the external and inertial loads;
- the construction of $\mathbf{H}_{MB}$ and $\mathbf{C}$.

The details on each step may be found in Wuillaume (2019).

3. Cable modeling

The numerical simulation of a lowering operation requires to model the cable which links the barge with its payload. To do so, the cable is discretized into cable elements and nodes where the mass is concentrated. Nodes are connected by spring-damper systems. When this approach is based on Cartesian coordinates, it is named the lumped mass method (Masciola et al., 2014; Hall and Goupee, 2015). The Composite-Rigid-Body Algorithm may be also used to simulate cables with the same modeling. Each cable element is composed of three joints to ensure two rotations at the position of the node and one translation to take into account the stretching along the cable element linked to the node. Thus two revolute joints and one prismatic joint are used. The bending and the torsion of the cable are neglected. Consequently, the internal loads are only present in the prismatic joint. For the joint j, they are defined by (Wuillaume et al., 2017):

$$\Gamma_j = \begin{cases} -\dfrac{EA}{L_u}(q_j + L_u) - \dfrac{CA}{L_u}\dot{q}_j & \text{if } |q_j| \geqslant L_u \\ -\dfrac{CA}{L_u}\dot{q}_j & \text{otherwise} \end{cases} \tag{11}$$

with E, C, A and L_u the Young's modulus, the damping coefficient, the cross sectional area of the cable and its unstretched length.

The lumped mass method and the cable modeling using the *CRBA* were compared by Wuillaume et al. (2017) and found identical.

As the payload is lowered, a winch is also necessary. During the pay-out, the unstretched length of the cable element connecting to the winch (located at the crane tip) is increased. The lowering velocity is assumed constant. Once the cable length is assumed too long, the first element is divided into two elements, as presented in Figure 3. Thus the cable element linked to the winch is a variable-length element while the other ones are constant-length elements. The cable loads of the variable-length element become:

$$\Gamma_j = \begin{cases} -\dfrac{EA}{L_u(t)}(q_j + L_u(t)) - \dfrac{CA}{L_u(t)}(\dot{q}_j + v_d(t)) & \text{if } |q_j| \geqslant L_u(t) \\ -\dfrac{CA}{L_u(t)}(\dot{q}_j + v_d(t)) & \text{otherwise} \end{cases} \tag{12}$$

with v_d the deployment velocity, which is negative for a lowering operation.

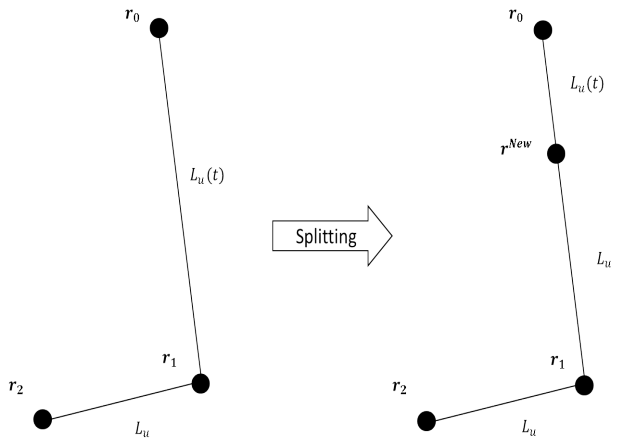

Figure 3: Sketch of a cable splitting during the pay-out of a cable. The vectors $\mathbf{r}$ represent the position of the nodes. The winch is at the node 0.

4. Governing fluid equations

The fluid is assumed incompressible and inviscid whereas the flow is considered as irrotational. Thereby, the fluid problem is solved in the frame of the potential flow theory. The velocity field results from a scalar velocity potential:

$$\mathbf{v} = \nabla\phi \tag{13}$$

The velocity potential, respectively the wave elevation, is decomposed as an unknown scattered (perturbation) component ϕ^P and a known incident component ϕ^I, respectively η^P and η^I:

$$\begin{cases} \phi = \phi^I + \phi^P \\ \eta = \eta^I + \eta^P \end{cases} \tag{14}$$

The incident wave field is based on the Airy wave theory:

$$\phi^I = \frac{Ag}{\omega}\frac{\cosh[k(z+h)]}{\cosh(kh)}\sin[k(x\cos(\beta)+y\sin(\beta)) - \omega t] \tag{15}$$

where A, ω, k and β represent the wave amplitude, the wave frequency, the wave number and the wave angle of the wave.

The weak-scatterer hypothesis assumes the perturbed quantities have to be small compared to the incident quantities:

$$\begin{cases} \phi^P \ll \phi^I \\ \eta^P \ll \eta^I \end{cases} \tag{16}$$

ϕ^P satisfies the Laplace's equation:

$$\Delta\phi^P = 0 \tag{17}$$

By using the Green's second identity, the integral equation arises:

$$\begin{aligned} -\phi^P(\mathbf{x}_i)\Omega(\mathbf{x}_i) - \iint_S \phi^P(\mathbf{x}_j)\frac{\partial G}{\partial n_j}(\mathbf{x}_i,\mathbf{x}_j)\,dS \\ + \iint_S G(\mathbf{x}_i,\mathbf{x}_j)\frac{\partial \phi^P}{\partial n}(\mathbf{x}_j)\,dS = 0 \end{aligned} \tag{18}$$

where $\mathbf{x}_i$ and $\mathbf{x}_j$ are two points of $\mathbb{R}^3$. $\Omega(\mathbf{x}_i)$ is the solid angle at the point $\mathbf{x}_i$. S denotes the boundary of the fluid domain. G is the Rankine source Green's function.

The discretization of Eq. (18) at every node of the mesh leads to:

$$\mathbf{G}\boldsymbol{\phi}^P = \mathbf{H}\boldsymbol{\phi}_n^P \tag{19}$$

where $\mathbf{G}$ and $\mathbf{H}$ are the influence matrices. Their expression are given in Letournel et al. (2018). $\boldsymbol{\phi}^P$ and $\boldsymbol{\phi}_n^P$ are the velocity potential and normal velocity vectors of size the number of nodes in the mesh.

The no-flux condition through the body surfaces leads to the following body condition:

$$\frac{\partial \phi^P}{\partial n} = -\frac{\partial \phi^I}{\partial n} + \mathbf{v}^{Solid}\cdot\mathbf{n} \quad \text{on } S_B(t) \tag{20}$$

The far field condition is:

$$\begin{cases} \phi^P \xrightarrow[r\to+\infty]{} 0 \\ \eta^P \xrightarrow[r\to+\infty]{} 0 \end{cases} \tag{21}$$

The velocity potential and its normal-derivative are obtained from the first boundary value problem (*BVP*) constituted of Eq. (19), (20) and (21) and the free surface boundary conditions.

At $t = 0$ s, the flow is assumed to be at rest. The initial condition on the scattererd components is:

$$\begin{cases} \phi^P = 0 \\ \eta^P = 0 \end{cases} \tag{22}$$

To avoid the generation of non-physical and spurious waves due to the abrupt appearance of the bodies in the flow, a ramp function is applied on the body condition:

$$f(t) = \begin{cases} 0 & \text{when } t \leqslant T_1 \\ 1 & \text{when } t \geqslant T_2 \\ \frac{1}{2}\left[1 - \cos\left(\pi\frac{t-T_1}{T_2-T_1}\right)\right] & \text{otherwise} \end{cases} \tag{23}$$

with T_1 and T_2 the starting and final time of application of the ramp function.

The application of the weak-scatterer hypothesis in the Bernoulli's equation gives the following expression of the pressure:

$$p = -\rho\left(\dot{\phi}^I + \dot{\phi}^P + \frac{1}{2}\nabla\phi^I\cdot\nabla\phi^I + \nabla\phi^I\cdot\nabla\phi^P + gz\right) \tag{24}$$

Then, the hydrodynamic loads on body j at its center of gravity ${}^e\mathbf{S}_j$ in the global frame Σ_e are:

$${}^e\mathbf{F}_j^{WSC} = \begin{pmatrix} -\iint_{S_{B_j}(t)} p\mathbf{n}\,dS \\ -\iint_{S_{B_j}(t)} p(\mathbf{x} - {}^e\mathbf{S}_j)\times\mathbf{n}\,dS \end{pmatrix} \tag{25}$$

with S_{B_j} the wetted surface of body j and $\mathbf{n}$ the inward normal vector.

The time-derivative of the scattered velocity potential, present in Eq. (24), is computed by solving a second Boundary Value Problem (Letournel et al., 2018). The integral equation of the second *BVP* becomes:

$$\mathbf{G}\dot{\boldsymbol{\phi}} = \mathbf{H}\dot{\boldsymbol{\phi}}_n \tag{26}$$

The time-derivative of the velocity potential $\dot{\phi}^P$ is known on the free surface from the free surface boundary equations and on the body surfaces from the time-derivative of the body condition (Letournel et al., 2017). After discretization, it comes for body j:

$$\dot{\boldsymbol{\phi}}_n^P(B_j) = -\dot{\boldsymbol{\phi}}_n^I(B_j) + \mathbf{C}\mathbf{K}_j\ddot{\boldsymbol{\eta}}_j + \mathbf{Q}_j \tag{27}$$

$\ddot{\boldsymbol{\eta}}_j$ represents the Cartesian acceleration of body j at its center of gravity and expressed in Σ_e. The expressions of the matrix $\mathbf{C}\mathbf{K}_j$ and the vector $\mathbf{Q}_j$ are given in Letournel (2015).

The motion equation expressed in Σ_e (by considering the hydrodynamic loads only) is used to close the system of differential equations:

$${}^e\mathbf{M}_j\ddot{\boldsymbol{\eta}}_j = {}^e\,\mathbf{F}_j^{WSC} \tag{28}$$

where ${}^e\mathbf{M}_j$ is the mass matrix of the body j.

The discretization of the hydrodynamic loads leads to (Wuillaume, 2019):

$${}^e\mathbf{F}_j^{WSC} = {}^e\mathbf{C}\mathbf{T}_j\dot{\boldsymbol{\phi}}^P(B_j) + {}^e\mathbf{T}_j^{WSC} \tag{29}$$

The expressions of the matrix ${}^e\mathbf{C}\mathbf{T}_j$ and the vector ${}^e\mathbf{T}_j^{WSC}$ are given in Letournel (2015).

Finally, the second Boundary Value Problem used to solve the wave-structure interaction is formed of Eq. (26), (27), (28) and (29). These governing equations are used in the numerical tool *WS_CN*. More details may be found in Wuillaume (2019).

5. Coupling equation of the wave-structure interaction

Two main strategies for solving multiphysics problems, such as wave-structure problems, exist: monolithic approach and partitioned approach (Felippa et al., 2001). With a monolithic approach, the governing differential equations are time-stepped simultaneously in a single numerical tool. This system of differential equations is called the coupling equation. The advantages of a monolithic approach are the robustness and the accuracy. But this approach involves a complex assembling and solving of the set of equations. A distinction is made between a monolithic formulation where a new numerical tool is created *ex nihilo*, including all the solvers, and a tight coupling in which different independent subsystems solving a unique field of the physics are linked through a coupling equation and time-stepped simultaneously.

Tight couplings are part of the partitioned approach (Gasmi et al., 2013). With such an approach, each field of the physics is treated in isolation. If the governing equations are separately stepped in time, the coupling is loose, otherwise it is tight. The main advantage of the partitioned approach is the inherent modularity. Tight coupling also have the advantages of the monolithic approach and their drawbacks. Loose couplings allows fitting the time step, the time integrator and more generally the physical model for every field solver. The main drawbacks are the stability problems due to the time lag between the time integrations of the field solvers. It results in an artificial increase or decrease of the energy in the system which leads to a loss of accuracy (Piperno and Farhat, 2001). Loose couplings may be split between explicit or sequential couplings and implicit or iterative couplings. By using a retroactive loop, an implicit coupling leads to the same results as a monolithic approach, other things being equal. Figure 4 summarized the main strategies of multiphysics problem solving.

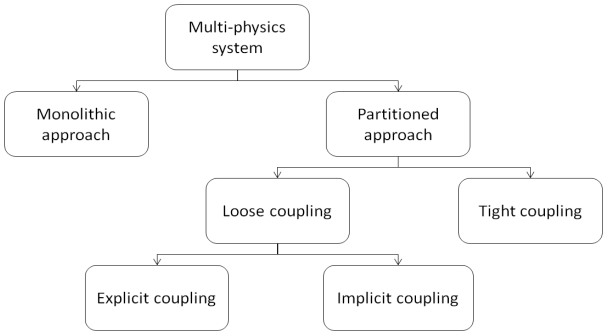

Figure 4: Main coupling strategies

To reach a robust, stable and accurate coupling while creating a modular architecture, a tight coupling between the Composite-Rigid-Body Algorithm and the weak-scatterer approach is chosen. Consequently, it is necessary to solve both the mechanical and fluid governing equations at the same time. It requires the introduction of the hydrodynamic loads Eq. (29) in the multibody motion equation Eq. (4) and the expression of the body condition Eq. (27) with respect to the articular acceleration $\ddot{\mathbf{q}}$. The integral equation Eq. (26) of the second Boundary Value Problem stays unchanged.

5.1. Multibody motion equation

The introduction of the hydrodynamic loads Eq. (29) in the multibody motion equation Eq. (4) leads to:

$$\mathbf{H}_{MB}\begin{pmatrix} {}^0\dot{\mathbf{V}}_0 \\ \ddot{\mathbf{q}} \end{pmatrix} = \begin{pmatrix} \mathbf{0}_{6\times1} \\ \boldsymbol{\Gamma} \end{pmatrix} - \mathbf{C} + \begin{pmatrix} {}^0\mathbf{F}^{WSC} \\ \boldsymbol{\Gamma}^{WSC} \end{pmatrix} \tag{30}$$

${}^0\mathbf{F}^{WSC}$ is the sum of all hydrodynamic loads acting on the whole multibody system at $\mathbf{O}_0$ and projected in the base frame:

$${}^0\mathbf{F}^{WSC} = \sum_{j\in\mathcal{F}^{WSC}} {}^0\mathbf{N}_e^j \, {}^e\mathbf{G}_j \, {}^e\mathbf{F}_j^{WSC} \tag{31}$$

with:

- $\mathcal{F}^{WSC}$ the set of the bodies subject to hydrodynamic loads. Each hydrodynamic body has a number in the multibody system and a number in $\mathcal{F}^{WSC}$. There is:

$$card(\mathcal{F}^{WSC}) = N^{WSC} \tag{32}$$

  $card(*)$ represents the number of elements of a set and N^{WSC} the number of bodies subject to hydrodynamics loads.

- ${}^e\mathbf{F}_j^{WSC}$ the hydrodynamic loads acting on the body j at $\mathbf{G}_j$ in Σ_e given by Eq. (29);

- ${}^e\mathbf{G}_j$ the (6×6) matrix to change the point of computation of the hydrodynamic loads from $\mathbf{G}_j$ to $\mathbf{O}_j$:

$${}^e\mathbf{G}_j = \begin{pmatrix} \mathbf{I}_3 & \mathbf{0}_{3\times3} \\ \mathbf{S}({}^e\mathbf{R}_j \, {}^j\mathbf{S}_j) & \mathbf{I}_3 \end{pmatrix} \tag{33}$$

- ${}^0\mathbf{N}_e^j$ the (6×6) matrix to project the hydrodynamic loads into the base frame from $\mathbf{O}_j$ to $\mathbf{O}_0$:

$${}^0\mathbf{N}_e^j = \begin{pmatrix} {}^0\mathbf{R}_e & \mathbf{0}_{3\times3} \\ \mathbf{S}({}^0\mathbf{P}_j){}^0\mathbf{R}_e & {}^0\mathbf{R}_e \end{pmatrix} \tag{34}$$

$\boldsymbol{\Gamma}^{WSC}$ is the sum of the hydrodynamic articular loads:

$$\boldsymbol{\Gamma}^{WSC} = \sum_{j\in\mathcal{F}^{WSC}\setminus\{0\}} \boldsymbol{\Gamma}_j^{WSC} \tag{35}$$

where $\boldsymbol{\Gamma}_j^{WSC}$ is the projection of the hydrodynamic loads acting on the body j into the articular space (Featherstone, 2008):

$$\boldsymbol{\Gamma}_j^{WSC} = {}^j\mathbf{J}_j^T \, {}^j\boldsymbol{\rho}_e \, {}^e\mathbf{G}_j \, {}^e\mathbf{F}_j^{WSC} \tag{36}$$

with:

- ${}^j\boldsymbol{\rho}_e$ the (6×6) projection matrix of the hydrodynamic loads from Σ_e to Σ_j:

$${}^j\boldsymbol{\rho}_e = \begin{pmatrix} {}^j\mathbf{R}_e & \mathbf{0}_{3\times3} \\ \mathbf{0}_{3\times3} & {}^j\mathbf{R}_e \end{pmatrix} \tag{37}$$

- ${}^{j}\mathbf{J}_j$ the $(6 \times n)$ Jacobian matrix of the body j, defined by:

$$ {}^{j}\mathbf{V}_j = {}^{j}\mathbf{T}_0 \, {}^{0}\mathbf{V}_0 + {}^{j}\mathbf{J}_j \, \dot{\mathbf{q}} \tag{38} $$

The Jacobian matrix represents the mapping between the operating space (using Cartesian coordinates) and the articular space (using articular variables). If the base is fixed, the kth column of ${}^{j}\mathbf{J}_j$ represents the contribution of the kth articular velocity to the Cartesian velocity ${}^{j}\mathbf{V}_j$. Following this definition, the Jacobian matrix does not exist for the base ($j = 0$).

Eq. (30) becomes:

$$ \begin{aligned} \mathbf{H}_{MB} \begin{pmatrix} {}^{0}\dot{\mathbf{V}}_0 \\ \ddot{\mathbf{q}} \end{pmatrix} - \begin{pmatrix} \sum\limits_{j \in \mathcal{F}^{WSC}} {}^{0}\mathbf{N}_e^{j} \, {}^{e}\mathbf{G}_j \, {}^{e}\mathbf{C}\mathbf{T}_j \, \dot{\boldsymbol{\phi}}^{P}(B_j) \\ \sum\limits_{j \in \mathcal{F}^{WSC} \setminus \{0\}} {}^{j}\mathbf{J}_j^{T} \, {}^{j}\boldsymbol{\rho}_e \, {}^{e}\mathbf{G}_j \, {}^{e}\mathbf{C}\mathbf{T}_j \, \dot{\boldsymbol{\phi}}^{P}(B_j) \end{pmatrix} \\ = \begin{pmatrix} \mathbf{0}_{6\times1} \\ \boldsymbol{\Gamma} \end{pmatrix} - \mathbf{C} + \begin{pmatrix} \sum\limits_{j \in \mathcal{F}^{WSC}} {}^{0}\mathbf{N}_e^{j} \, {}^{e}\mathbf{G}_j \, {}^{e}\mathbf{T}_j^{WSC} \\ \sum\limits_{j \in \mathcal{F}^{WSC} \setminus \{0\}} {}^{j}\mathbf{J}_j^{T} \, {}^{j}\boldsymbol{\rho}_e \, {}^{e}\mathbf{G}_j \, {}^{e}\mathbf{T}_j^{WSC} \end{pmatrix} \end{aligned} \tag{39} $$

5.2. Body condition

The body condition Eq. (27) is expressed with respect to the Cartesian accelerations $\ddot{\boldsymbol{\eta}}_j$ whereas the motion equation Eq. (39) is based on the articular accelerations $\ddot{\mathbf{q}}$. In order to form a linear system, it is necessary to use the same unknowns, namely the articular accelerations because they are a reduced set of coordinates. To do so, the first step is to write the Cartesian velocity with respect to the velocity of the base and the articular velocities. The angular velocity of the body ${}^{e}\boldsymbol{\omega}_j$ in Σ_e depends on the time-derivative of the Cardan angles:

$$ {}^{e}\boldsymbol{\omega}_j = \mathbf{S}_j \begin{pmatrix} \dot{\varphi}_j \\ \dot{\theta}_j \\ \dot{\psi}_j \end{pmatrix} \tag{40} $$

with:

$$ \mathbf{S}_j = \begin{pmatrix} \cos(\theta_j)\cos(\psi_j) & -\sin(\psi_j) & 0 \\ \cos(\theta_j)\sin(\psi_j) & \cos(\psi_j) & 0 \\ -\sin(\theta_j) & 0 & 1 \end{pmatrix} \tag{41} $$

${}^{e}\mathbf{V}_j$ is the Cartesian velocity of body j at $\mathbf{O}_j$ with respect to Σ_e. $\dot{\boldsymbol{\eta}}_j$ is expressed at $\mathbf{G}_j$ and using the Cardan angles. ${}^{e}\mathbf{V}_j$ and $\dot{\boldsymbol{\eta}}_j$ are related by:

$$ \dot{\boldsymbol{\eta}}_j = \boldsymbol{\tau}_j^{-1} \, {}^{e}\mathbf{V}_j \tag{42} $$

with:

$$ \boldsymbol{\tau}_j^{-1} = \begin{pmatrix} \mathbf{I}_3 & -\mathbf{S}({}^{e}\mathbf{R}_j \, {}^{j}\mathbf{S}_j) \\ \mathbf{0}_{3\times3} & \mathbf{S}_j^{-1} \end{pmatrix} \tag{43} $$

The $(6\times(n+6))$ generalized Jacobian matrix ${}^{e}\boldsymbol{\Lambda}_j$ allows to relate the (6×1) velocity vector of body j in Σ_e to the base and articular velocities:

$$ {}^{e}\mathbf{V}_j = {}^{e}\boldsymbol{\Lambda}_j \begin{pmatrix} {}^{0}\mathbf{V}_0 \\ \dot{\mathbf{q}} \end{pmatrix} \tag{44} $$

The kth column of ${}^{e}\boldsymbol{\Lambda}_j$ represents the contribution of the kth component of the base velocity ${}^{0}\mathbf{V}_0$, if $k \leqslant 6$, or the kth, if $k > 6$, articular velocity to the Cartesian velocity ${}^{e}\mathbf{V}_j$.

After time-differentiation of Eq. (44) and Eq. (42) and the introduction of Eq. (67), the Cartesian acceleration, $\ddot{\boldsymbol{\eta}}_j$, can be expressed as function of the base and articular accelerations:

$$ \begin{aligned} \ddot{\boldsymbol{\eta}}_j = \dot{\boldsymbol{\tau}}_j^{-1} \, {}^{e}\boldsymbol{\Lambda}_j \begin{pmatrix} {}^{0}\mathbf{V}_0 \\ \dot{\mathbf{q}} \end{pmatrix} + \boldsymbol{\tau}_j^{-1} \, {}^{e}\dot{\boldsymbol{\Lambda}}_j \begin{pmatrix} {}^{0}\mathbf{V}_0 \\ \dot{\mathbf{q}} \end{pmatrix} \\ + \boldsymbol{\tau}_j^{-1} \, {}^{e}\boldsymbol{\Lambda}_j \left[\begin{pmatrix} {}^{0}\dot{\mathbf{V}}_0 \\ \ddot{\mathbf{q}} \end{pmatrix} - \begin{pmatrix} \begin{pmatrix} \mathbf{S}({}^{0}\boldsymbol{\omega}_0) \, {}^{0}\mathbf{v}_0 \\ \mathbf{0}_{3\times1} \end{pmatrix} \\ \mathbf{0}_{n\times1} \end{pmatrix} \right] \end{aligned} \tag{45} $$

The time-derivation of $\boldsymbol{\tau}_j^{-1}$ is expressed by:

$$ \dot{\boldsymbol{\tau}}_j^{-1} = \begin{pmatrix} \mathbf{0}_{3\times3} & -{}^{e}\mathbf{R}_j \, \mathbf{S}({}^{j}\boldsymbol{\omega}_j) \mathbf{S}({}^{j}\mathbf{S}_j) \, {}^{j}\mathbf{R}_e \\ \mathbf{0}_{3\times3} & -\mathbf{S}_j^{-1} \dot{\mathbf{S}}_j \mathbf{S}_j^{-1} \end{pmatrix} \tag{46} $$

Finally, the introduction of Eq. (45) in Eq. (27) yields:

$$ \begin{aligned} \dot{\boldsymbol{\phi}}_n^{P}(B_j) = -\dot{\boldsymbol{\phi}}_n^{I}(B_j) + \mathbf{C}\mathbf{K}_j \boldsymbol{\tau}_j^{-1} \, {}^{e}\boldsymbol{\Lambda}_j \begin{pmatrix} {}^{0}\dot{\mathbf{V}}_0 \\ \ddot{\mathbf{q}} \end{pmatrix} \\ + \mathbf{C}\mathbf{K}_j (\dot{\boldsymbol{\tau}}_j^{-1} \, {}^{e}\boldsymbol{\Lambda}_j + \boldsymbol{\tau}_j^{-1} \, {}^{e}\dot{\boldsymbol{\Lambda}}_j) \begin{pmatrix} {}^{0}\mathbf{V}_0 \\ \dot{\mathbf{q}} \end{pmatrix} \\ - \mathbf{C}\mathbf{K}_j \boldsymbol{\tau}_j^{-1} \, {}^{e}\boldsymbol{\Lambda}_j \begin{pmatrix} \begin{pmatrix} \mathbf{S}({}^{0}\boldsymbol{\omega}_0) \, {}^{0}\mathbf{v}_0 \\ \mathbf{0}_{3\times1} \end{pmatrix} \\ \mathbf{0}_{n\times1} \end{pmatrix} + \mathbf{Q}_j \end{aligned} \tag{47} $$

It remains to clarify the expressions of the Jacobian matrix ${}^{j}\mathbf{J}_j$, the generalized Jacobian matrix ${}^{e}\boldsymbol{\Lambda}_j$ and its time-differentiation ${}^{e}\dot{\boldsymbol{\Lambda}}_j$.

5.3. Jacobian matrices

From the definition of the Jacobian matrices, let us consider the kth articulation of a multibody system and a body j such as $j > k$. The base is assumed motionless. The articular velocity $\dot{q}_k$ leads to a velocity vector ${}^{k}\mathbf{V}_j^{k}$ for the body j:

$$ {}^{k}\mathbf{V}_j^{k} = \begin{pmatrix} \left[\sigma_k \, {}^{k}\mathbf{z}_k + \bar{\sigma}_k ({}^{k}\mathbf{z}_k \times {}^{k}\mathbf{P}_j) \right] \dot{q}_k \\ \bar{\sigma}_k \, {}^{k}\mathbf{z}_k \, \dot{q}_k \end{pmatrix} \tag{48} $$

By summing the contributions of all the joints of the direct branch $\beta(j)$ containing the set of bodies on the direct branch between the base (not included) and the body j (included), one can have:

$$ \mathbf{V}_j = \sum_{k \in \beta(j)} {}^{k}\mathbf{V}_j^{k} \tag{49} $$

$$ = \begin{pmatrix} \sum\limits_{k \in \beta(j)} \left[\sigma_k \, {}^{k}\mathbf{z}_k + \bar{\sigma}_k ({}^{k}\mathbf{z}_k \times {}^{k}\mathbf{P}_j) \right] \dot{q}_k \\ \sum\limits_{k \in \beta(j)} \bar{\sigma}_k \, {}^{k}\mathbf{z}_k \, \dot{q}_k \end{pmatrix} \tag{50} $$

It is necessary to define a common frame of projection, for instance Σ_j:

$$ {}^{j}\mathbf{V}_j = \begin{pmatrix} \sum\limits_{k\in\beta(j)} \left[\sigma_k\, {}^{j}\mathbf{z}_k + \bar{\sigma}_k \mathbf{S}({}^{j}\mathbf{z}_k)\, {}^{j}\mathbf{R}_k\, {}^{k}\mathbf{P}_j\right]\dot{q}_k \\ \sum\limits_{k\in\beta(j)} \bar{\sigma}_k\, {}^{j}\mathbf{z}_k\, \dot{q}_k \end{pmatrix} \tag{51} $$

Thus, following the matrix format of Eq. (38), the expression of ${}^{j}\mathbf{J}_j$ is:

$$ col_k({}^{j}\mathbf{J}_j) = \begin{cases} \begin{pmatrix} \left[\sigma_k\, {}^{j}\mathbf{z}_k + \bar{\sigma}_k \mathbf{S}({}^{j}\mathbf{z}_k)\, {}^{j}\mathbf{R}_k\, {}^{k}\mathbf{P}_j\right]\dot{q}_k \\ \bar{\sigma}_k\, {}^{j}\mathbf{z}_k\, \dot{q}_k \end{pmatrix} & \text{if } k \in \beta(j) \\ \mathbf{0}_{6\times 1} & \text{if } k \notin \beta(j) \end{cases} \tag{52} $$

The change of frames is achieved using the projection matrix Eq. (37), for instance in the base frame:

$$ {}^{0}\mathbf{J}_j = {}^{0}\boldsymbol{\rho}_j\, {}^{j}\mathbf{J}_j \tag{53} $$

5.4. Expression of ${}^{e}\boldsymbol{\Lambda}_j$

The projection in Σ_e of Eq. (38) leads to:

$$ {}^{e}\mathbf{V}_j = {}^{e}\boldsymbol{\rho}_0 \left({}^{0}\mathbf{L}_j\, {}^{0}\mathbf{V}_0 + {}^{0}\mathbf{J}_j\, \dot{\mathbf{q}} \right) \tag{54} $$

where:

- ${}^{0}\mathbf{L}_j$ changes the point of computation of ${}^{0}\mathbf{V}_0$ from $\mathbf{O}_0$ to $\mathbf{O}_j$:

$$ {}^{0}\mathbf{L}_j = \begin{pmatrix} \mathbf{I}_3 & -\mathbf{S}({}^{0}\mathbf{P}_j) \\ \mathbf{0}_{3\times 3} & \mathbf{I}_3 \end{pmatrix} \tag{55} $$

- the expression of ${}^{0}\mathbf{J}_j$ is given by Eq. (53).

Based on Eq. (44), the expression of the generalized Jacobian matrix is:

$$ {}^{e}\boldsymbol{\Lambda}_j = \begin{cases} {}^{e}\boldsymbol{\rho}_0 \begin{pmatrix} {}^{0}\mathbf{L}_j & {}^{0}\mathbf{J}_j \end{pmatrix} & \text{if } j \neq 0 \\ {}^{e}\boldsymbol{\rho}_0 \begin{pmatrix} {}^{0}\mathbf{L}_j & \mathbf{0}_{6\times n} \end{pmatrix} & \text{if } j = 0 \end{cases} \tag{56} $$

5.5. Expression of ${}^{e}\dot{\boldsymbol{\Lambda}}_j$

The time-differentiation of Eq. (56) is challenging because of the Jacobian matrix ${}^{0}\mathbf{J}_j$. Two methods exist to compute the time-derivation of such a Jacobian matrix. The first one is a direct calculation as presented by Hourtash (2005). The drawback of this approach is its complexity. The second method is based on a recursive algorithm which computes ${}^{e}\dot{\boldsymbol{\Lambda}}_j \begin{pmatrix} {}^{0}\mathbf{V}_0 \\ \dot{\mathbf{q}} \end{pmatrix}$ instead of ${}^{e}\dot{\boldsymbol{\Lambda}}_j$ directly (Khalil and Chevallereau, 1987).

The time-derivative of Eq. (44) is:

$$ {}^{e}\dot{\mathbf{V}}_j = {}^{e}\dot{\boldsymbol{\Lambda}}_j \begin{pmatrix} {}^{0}\mathbf{V}_0 \\ \dot{\mathbf{q}} \end{pmatrix} + {}^{e}\boldsymbol{\Lambda}_j \left[\begin{pmatrix} {}^{0}\dot{\mathbf{V}}_0 \\ \ddot{\mathbf{q}} \end{pmatrix} - \begin{pmatrix} \mathbf{S}({}^{0}\boldsymbol{\omega}_0)\, {}^{0}\mathbf{v}_0 \\ \mathbf{0}_{3\times 1} \\ \mathbf{0}_{n\times 1} \end{pmatrix} \right] \tag{57} $$

Assuming ${}^{0}\dot{\mathbf{V}}_0 = \mathbf{0}_{6\times 1}$ and $\ddot{\mathbf{q}} = \mathbf{0}_{n\times 1}$ and applying Eq. (56):

$$ {}^{e}\dot{\mathbf{V}}_j^{*} = {}^{e}\dot{\boldsymbol{\Lambda}}_j \begin{pmatrix} {}^{0}\mathbf{V}_0 \\ \dot{\mathbf{q}} \end{pmatrix} - {}^{e}\boldsymbol{\rho}_0 \begin{pmatrix} \mathbf{S}({}^{0}\boldsymbol{\omega}_0)\, {}^{0}\mathbf{v}_0 \\ \mathbf{0}_{3\times 1} \end{pmatrix} \tag{58} $$

By denoting:

$$ {}^{e}\dot{\mathbf{V}}_j^{*} = {}^{e}\dot{\mathbf{V}}_j \Big|_{\substack{{}^{0}\dot{\mathbf{V}}_0 = \mathbf{0}_{6\times 1} \\ \ddot{\mathbf{q}} = \mathbf{0}_{n\times 1}}} \tag{59} $$

${}^{e}\dot{\mathbf{V}}_j^{*}$ can also be expressed by:

$$ {}^{e}\dot{\mathbf{V}}_j^{*} = {}^{e}\boldsymbol{\rho}_j\, {}^{j}\dot{\mathbf{V}}_j^{*} \tag{60} $$

The introduction of Eq. (60) in Eq. (58) gives:

$$ {}^{e}\dot{\boldsymbol{\Lambda}}_j \begin{pmatrix} {}^{0}\mathbf{V}_0 \\ \dot{\mathbf{q}} \end{pmatrix} = {}^{e}\boldsymbol{\rho}_j\, {}^{j}\dot{\mathbf{V}}_j^{*} + {}^{e}\boldsymbol{\rho}_0 \begin{pmatrix} \mathbf{S}({}^{0}\boldsymbol{\omega}_0)\, {}^{0}\mathbf{v}_0 \\ \mathbf{0}_{3\times 1} \end{pmatrix} \tag{61} $$

Using the assumption $\ddot{\mathbf{q}} = \mathbf{0}_{n\times 1}$ in Eq. (7) allows writing for $i = a_j$:

$$ {}^{j}\dot{\mathbf{V}}_j^{*} = {}^{j}\mathbf{T}_i\, {}^{i}\dot{\mathbf{V}}_i^{*} + {}^{j}\boldsymbol{\gamma}_j \tag{62} $$

While the hypothesis ${}^{0}\dot{\mathbf{V}}_0 = \mathbf{0}_{6\times 1}$ initializes this recursive equation:

$$ {}^{0}\dot{\mathbf{V}}_0^{*} = \mathbf{0}_{6\times 1} \tag{63} $$

Using Eq. (62) and (63), ${}^{j}\dot{\mathbf{V}}_j^{*}$ can be computed for each body during the Composite-Rigid-Body Algorithm. Then, the quantity ${}^{e}\dot{\boldsymbol{\Lambda}}_j \begin{pmatrix} {}^{0}\mathbf{V}_0 \\ \dot{\mathbf{q}} \end{pmatrix}$ can be calculated from Eq. (61).

Thereby:

$$ {}^{e}\dot{\boldsymbol{\Lambda}}_j \begin{pmatrix} {}^{0}\mathbf{V}_0 \\ \dot{\mathbf{q}} \end{pmatrix} = \begin{cases} \left\{ \begin{array}{l} {}^{e}\boldsymbol{\rho}_j\, {}^{j}\dot{\mathbf{V}}_j^{*} + {}^{e}\boldsymbol{\rho}_0 \begin{pmatrix} \mathbf{S}({}^{0}\boldsymbol{\omega}_0)\, {}^{0}\mathbf{v}_0 \\ \mathbf{0}_{3\times 1} \end{pmatrix} \\ \text{with:} \\ {}^{j}\dot{\mathbf{V}}_j^{*} = {}^{j}\mathbf{T}_i\, {}^{i}\dot{\mathbf{V}}_i^{*} + {}^{j}\boldsymbol{\gamma}_j \text{ for } i = a_j \\ {}^{0}\dot{\mathbf{V}}_0^{*} = \mathbf{0}_{6\times 1} \end{array} \right\} & \text{if } j \neq 0 \\ {}^{e}\boldsymbol{\rho}_0 \begin{pmatrix} \mathbf{S}({}^{0}\boldsymbol{\omega}_0)\, {}^{0}\mathbf{v}_0 \\ \mathbf{0}_{3\times 1} \end{pmatrix} & \text{if } j = 0 \end{cases} \tag{64} $$

5.6. Final linear system

The coupling equation between the Composite-Rigid-Body Algorithm and the weak-scatterer approach is formed of Eq. (26), (39) and (47) and leads to a linear system $\mathbf{AX} = \mathbf{B}$. The time-stepping is achieved using a fourth-order explicit Runge-Kutta scheme.

The Composite-Rigid-Body Algorithm is implemented in C++ in the numerical tool *InWave* while the weak-scatterer

approach is implemented in Fortran 90 in the solver *WS_CN*. Thus, a language binding is mandatory because of the two different programming languages. The co-simulation is driven in a Python environment. *Cython* makes the language binding between the C++ source code (Behnel et al., 2011) and the Python glue code whereas *f2py* does the same for the Fortran 90 source code (Peterson, 2009).

The creation and the solving of the tight wave-structure coupling along with the temporal loop of the co-simulation are achieved by a Python numerical tool named *InWaveS_CN*. Figure 5 presents the relationships between *InWave*, *WS_CN* and *InWaveS_CN*.

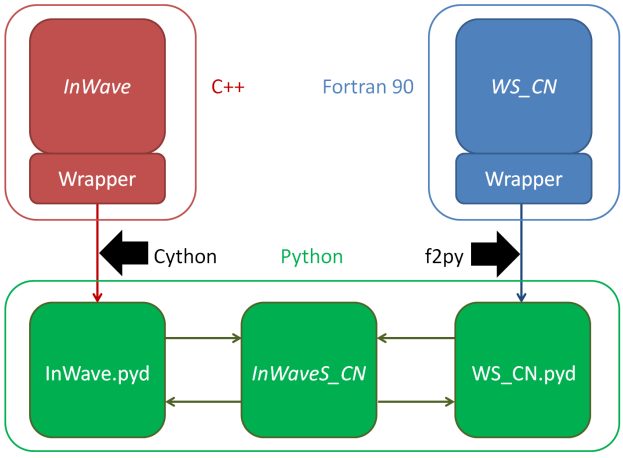

Figure 5: Language binding between *InWave* and *WS_CN* using Python as glue code language. The red, green and blue colors represent the C++, Python and Fortran languages.

The implementation of the tight coupling between *InWave* and *WS_CN* unfolds in five steps:

1. *InWave* performs the three stages of the Composite-Rigid-Body Algorithm while *WS_CN* solves the first boundary value problem;
2. The quantities, required for solving the wave-structure interaction, are sent to *InWaveS_CN*;
3. The linear system $\mathbf{AX} = \mathbf{B}$ is formed;
4. The iterative method *GMRES* is applied to solve the linear system;
5. The solution is assigned to the fluid and mechanical solvers, the multibody acceleration is expressed into the Cartesian space. The state vector of each solver is time-stepped.

Figure 6 presents the flow diagram of the five different steps. Only one stage of the fourth-order Runge-Kutta method is represented.

6. Lowering operation simulations

This part presents the application of the coupling between the Composite-Rigid-Algorithm and the weak-scatterer

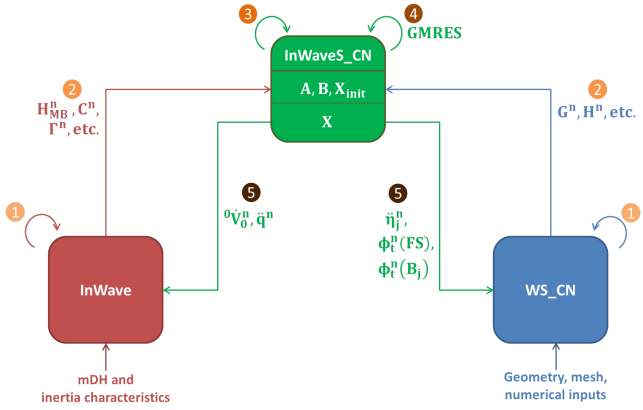

Figure 6: The five steps of the tight coupling between *InWave* and *WS_CN*. The red, green and blue colors represent the C++, Python and Fortran languages. The arrows denote the communication between the modules. The color of the arrows depends on the programming language which sends the data. The superscript n denotes the n^{th} time step.

approach through *InWaveS_CN* in the case of a lowering operation with an immersed payload and its comparison with *InWave* (Combourieu et al., 2014).

6.1. Crane barge and payload

A cylindrical floating crane barge is considered with a spherical payload connected to the crane tip by a cable. The geometrical and inertial properties of the barge and the payload are presented in Table 1. The center of gravity of the barge, respectively the payload, is at the center of the cylinder, respectively the sphere. The crane is considered as being part of the barge. The cable goes from the crane tip to the sphere center. Its mechanical properties are given in Table 2. The cable is considered as very stiff. Its mass and the hydrodynamic loads applying on it are neglected. The mechanical system formed by the barge and the payload are composed of 4 bodies: the base (numbered 0) and the three bodies necessary for modeling the cable. The payload is represented by the last body (numbered 3) which is also used for the cable.

Due to the presence of the payload, the barge has a static angle of 1.007° in pitch.

Table 1
Geometrical and inertial properties of the barge and the payload at their center of gravity

	Barge	Payload
Radius (m)	1	0.2
Height (m)	0.6	ø
Initial position (m)	$(-0.5, 0, 0)$	$(1.5, 0, -0.4)$
Mass (kg)	966.04	40
I_{xx} (kg m2)	270.49	0.64
I_{yy} (kg m2)	270.49	0.64
I_{zz} (kg m2)	483.02	0.64

Table 2
Mechanical properties of the cable

	Cable
Number of cable elements	1
Unstretched length (m)	2.9
Axial stiffness (N/m)	344816
Axial damping (N/m s)	344,8
Endpoint 1 (m)	(1.5, 0, 2.5)
Endpoint 2 (m)	(1.5, 0, −0.4)

6.2. Validation in seakeeping

This section presents the comparison between *InWave* and *InWaveS_CN* on the seakeeping of the barge and the payload connected by a cable in a regular wave field. These two numerical tools are based on the Composite-Rigid-Body Algorithm. Regarding the hydrodynamic theory, *InWave* uses *Nemoh* (Babarit and Delhommeau, 2015), the linear frequency-domain potential flow based solver of Ecole Centrale de Nantes whereas *InWaveS_CN* used the weak-scatterer approach of *WS_CN*. Therefore, the hydrodynamic theories along with the wave-structure couplings are different but the dynamics algorithms are identical. The incident wave field is a regular Airy wave of amplitude 1 mm, wave frequency 6.4 rad/s and coming from the positive y. The water density is 1025 kg/m^3 and the water depth 10 m. A ramp is applied for 15 s. The meshes used in *Nemoh* (for *InWave*) are shown in Figure 7, while the initial mesh used in *InWaveS_CN* is displayed in Figure 8. The simulation lasts 40 s. The comparison of the heave and pitch motion of the barge is presented in Figure 9. Once the steady state is reached, *InWave* and *InWaveS_CN* match as expected with a small steeness wave. This result validates the implementation of the coupling equation presented in the last section.

6.3. Lowering velocity rise

A lowering velocity rise is now applied to study the effect of the unsteadyness and the body nonlinearities in a lowering operation. The incident wave field stays identical to the one used in the seakeeping case. The lowering velocity is applied between $t = 5$s and $t = 35$s. The considered lowering velocity are: 0.0005 m/s, 0.0015 m/s, 0.003 m/s, 0.005 m/s, 0.008 m/s, 0.015 m/s, 0.025 m/s and 0.035 m/s. The comparison between *InWave* and *InWaveS_CN* are presented in Figure 10, Figure 11, Figure 12, Figure 13, Figure 14, Figure 15, Figure 16 and Figure 17, respectively. As all the simulations have the same duration, the more important the lowering velocity is, the deeper the payload goes down, the more important the distance is to the equilibrium position of the payload where the hydrodynamic database was computed. It can be seen that the weak-scatterer approach and the linear potential flow theory match as long as the payload is lowered on a small distance relative to its size. Thus, until a lowering velocity of 0.003 m/s, which represents a lowering distance of 0.45 time the radius of the payload, the two hydrodynamic theories agree. But, above this value, some differences appear. Progressively, a phase shift in pitch appears and also a

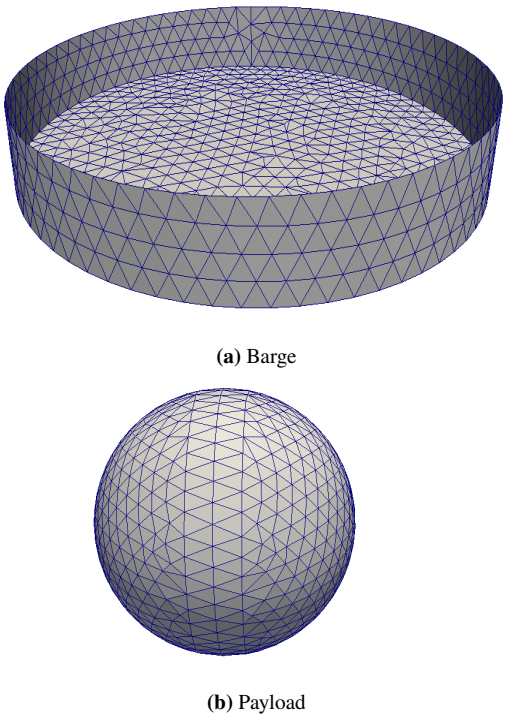

(a) Barge

(b) Payload

Figure 7: View of the initial meshes used in *InWave*

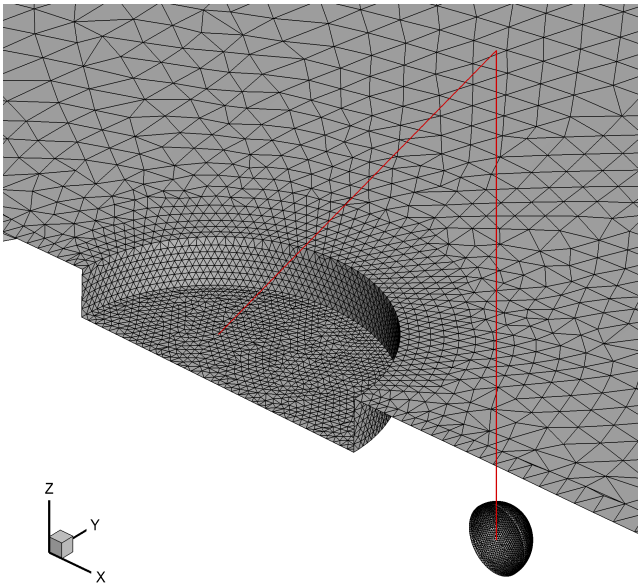

Figure 8: View of the initial mesh used in *InWaveS_CN*. The crane and the cable are in red.

difference on the heave and pitch amplitudes. These differences are due to the strong hypotheses of the linear potential flow theory used in *InWave* through *Nemoh*. In this classical modeling, it is assumed that the motions of the bodies have a small amplitude motion and the waves a small steepness. These hypotheses are violated in such lowering operations when the relative distances between the payload and

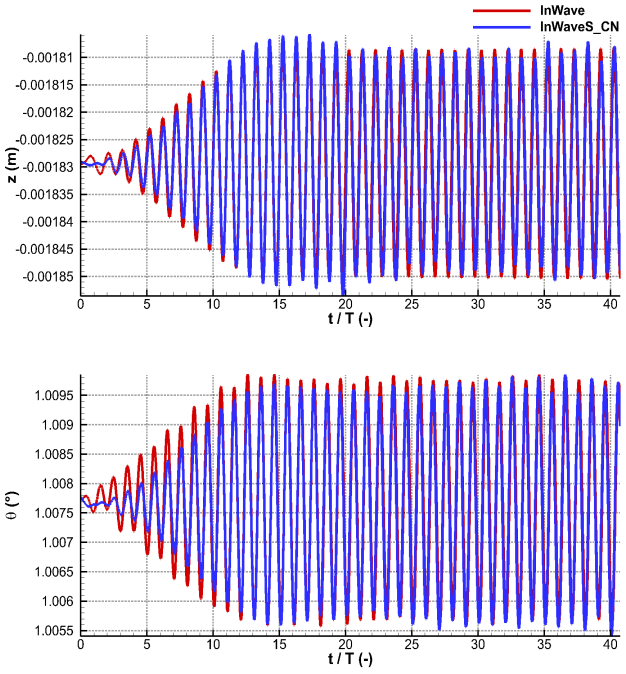

Figure 9: Comparison of time series of the heave (top) and pitch (bottom) motion of the barge without lowering velocity from the numerical results of *InWave* and *InWaveS_CN*

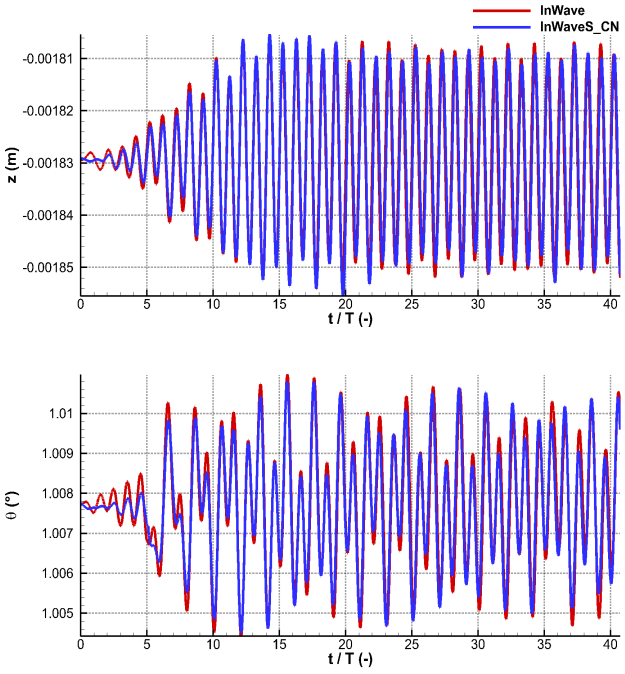

Figure 10: Comparison of time series of the heave (top) and pitch (bottom) motion of the barge with a lowering velocity of 0.0005 m/s from the numerical results of *InWave* and *InWaveS_CN*

the barge and between the payload and the free surface become important. Consequently, the added mass and damping coefficients of the payload are good as long as it is close to its equilibrium position and they become more and more inaccurate with a deeper and deeper lowering.

For the sake of illustration, the perturbed wave pattern obtained with *InWaveS_CN* for a lowering velocity of 0.025 m/s is displayed in Figure 18.

7. Conclusion

This paper describes the evaluation of the wave-structure interaction between a mechanical solver, *InWave*, based on the Composite-Rigid-Algorithm and a hydrodynamic solver, *WS_CN*, based on the weak-scatterer approach. The dynamics algorithm enables the simulation of multibody systems with mechanical interaction while the weak-scatterer approach allows to calculate the hydrodynamic interaction between bodies with large relative motions and large steepness waves. The coupling of this two solvers leads to the creation of a numerical tool, *InWaveS_CN*, which can simulate with consistency a lowering operation with a payload in the water.

The coupling is chosen as tight in order to preserve the modularity, the stability and the accuracy of the final solver. The derivation of the coupling equation between *InWave* and *WS_CN* is presented. It results from the introduction of the hydrodynamic loads into the multibody motion equation and the expression of the body condition with respect to the articular accelerations.

Once the coupling equation is established, *InWaveS_CN* is applied and compared to *InWave* in the case of lowering

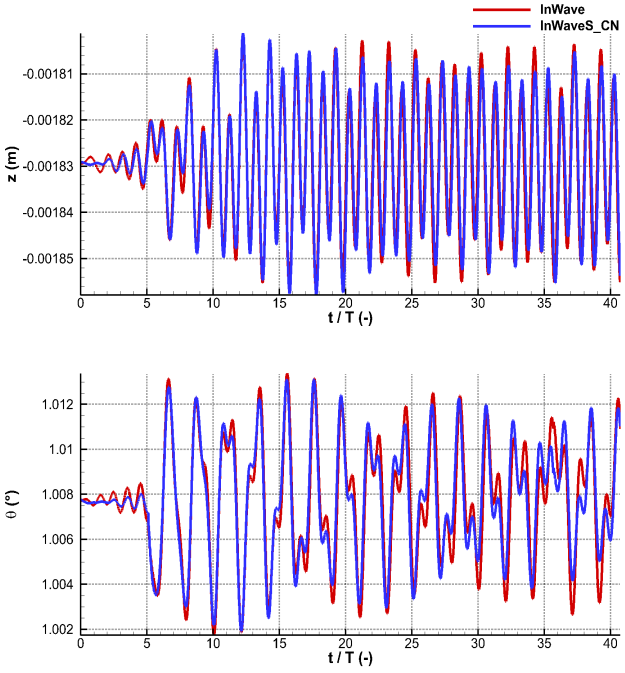

Figure 11: Comparison of time series of the heave (top) and pitch (bottom) motion of the barge with a lowering velocity of 0.0015 m/s from the numerical results of *InWave* and *InWaveS_CN*

operations with an immersed payload. The seakeeping with a zero lowering velocity shows a good agreement which validates the theory of the coupling equation. Then, a lowering

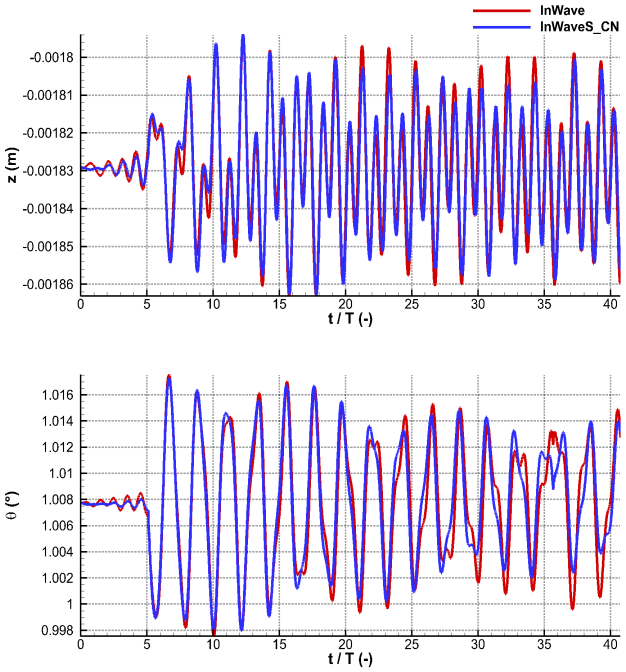

Figure 12: Comparison of time series of the heave (top) and pitch (bottom) motion of the barge with a lowering velocity of 0.003 m/s from the numerical results of *InWave* and *InWaveS_CN*

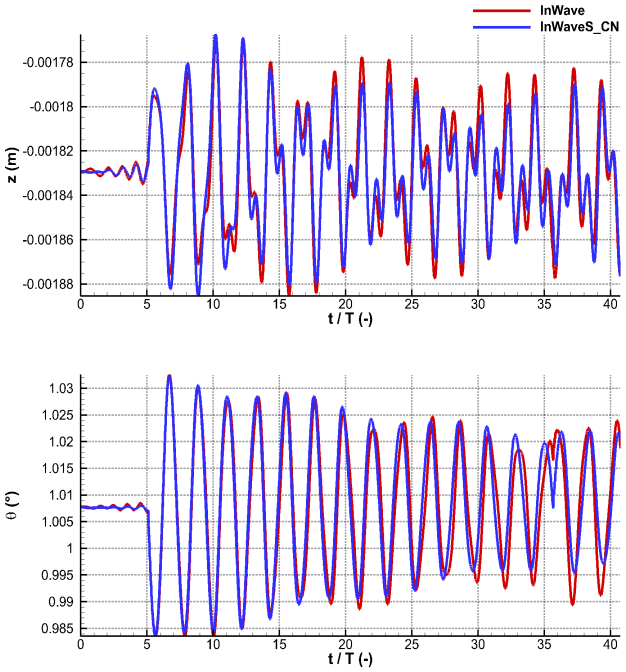

Figure 14: Comparison of time series of the heave (top) and pitch (bottom) motion of the barge with a lowering velocity of 0.008 m/s from the numerical results of *InWave* and *InWaveS_CN*

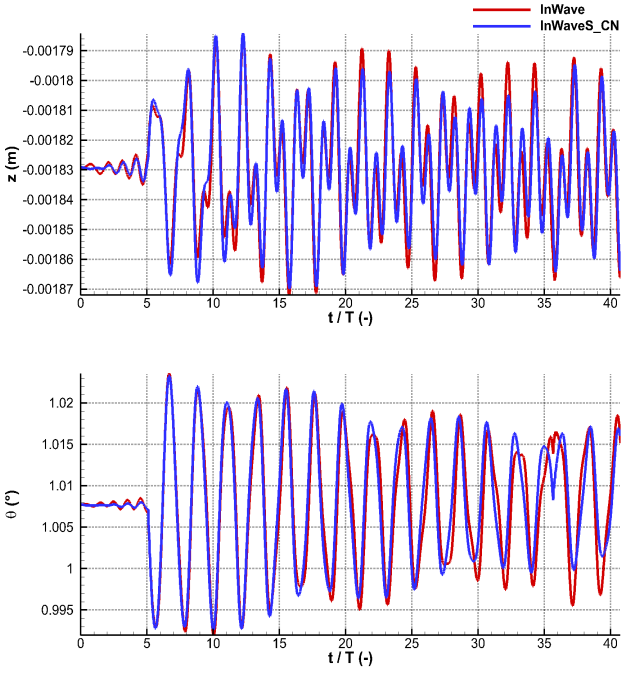

Figure 13: Comparison of time series of the heave (top) and pitch (bottom) motion of the barge with a lowering velocity of 0.005 m/s from the numerical results of *InWave* and *InWaveS_CN*

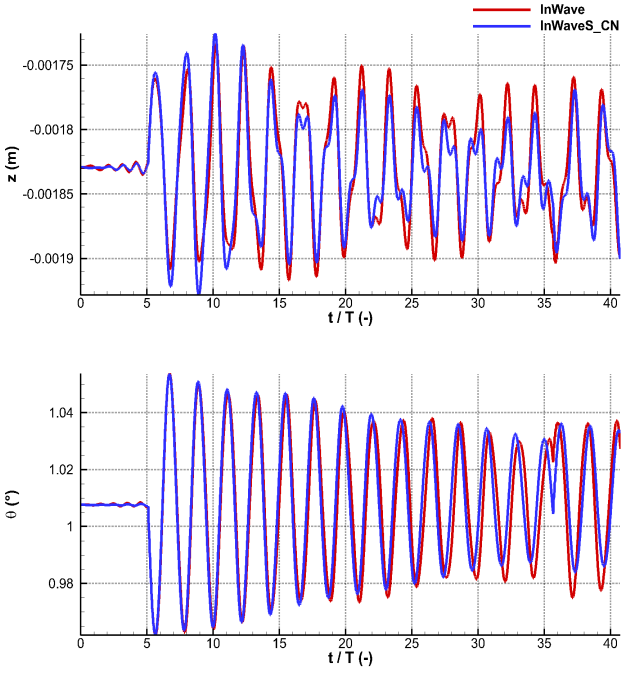

Figure 15: Comparison of time series of the heave (top) and pitch (bottom) motion of the barge with a lowering velocity of 0.015 m/s from the numerical results of *InWave* and *InWaveS_CN*

velocity rise is performed in order to distinguish the differences due to the hydrodynamic modeling. It appears that as long as the lowering velocity involves a small displacement of the payload with respect to its size, the two hydrodynamic theories match. Otherwise, some differences appear in terms of heave and pitch amplitudes and pitch phase shift. In this

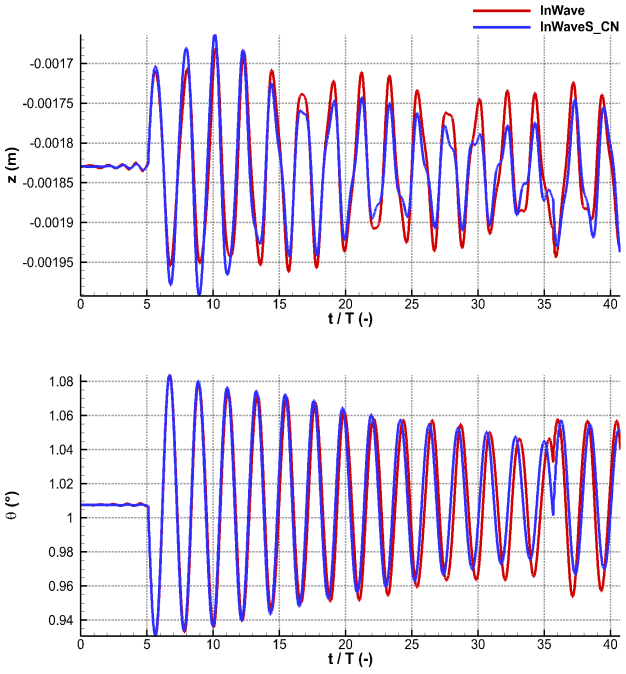

Figure 16: Comparison of time series of the heave (top) and pitch (bottom) motion of the barge with a lowering velocity of 0.025 m/s from the numerical results of *InWave* and *InWaveS_CN*

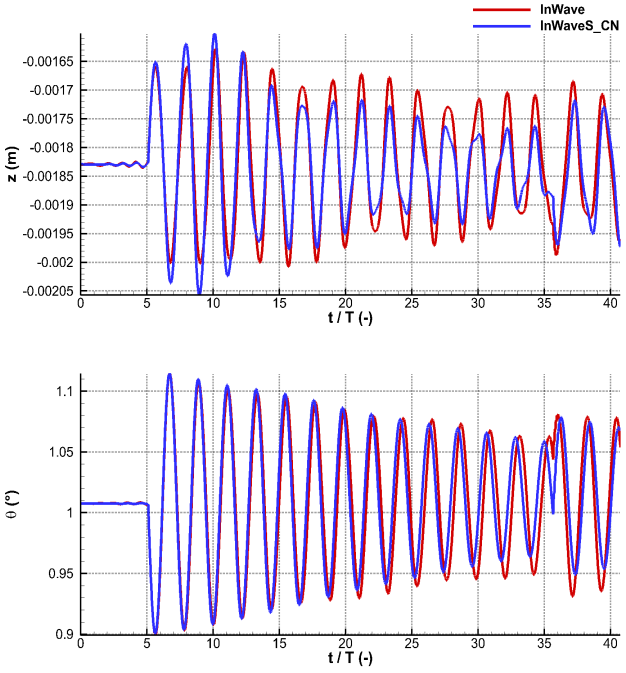

Figure 17: Comparison of time series of the heave (top) and pitch (bottom) motion of the barge with a lowering velocity of 0.035 m/s from the numerical results of *InWave* and *InWaveS_CN*

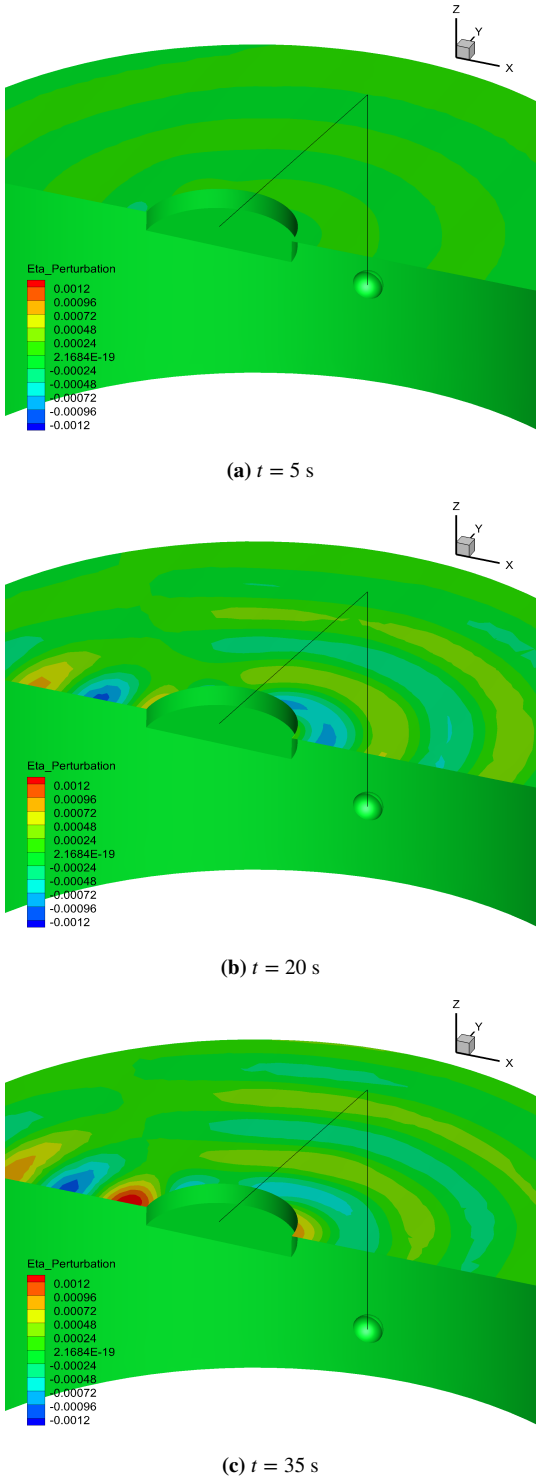

(a) $t = 5$ s

(b) $t = 20$ s

(c) $t = 35$ s

Figure 18: Perturbed component of the wave pattern (η^P) from the numerical results of *InWaveS_CN* for a lowering velocity of 0.025 m/s

condition, it is shown that the classical linear potential flow theory suffers of its strong assumptions of small body motion amplitude and small wave steepness. The use of a weakly or fully nonlinear potential flow based solver becomes necessary.

In this work, only the effect of the lowering velocity has been studied. Future work should consider the impact of other parameters such as the wave amplitude, the initial po-

sition of the payload with respect to the free surface and the barge, the possible gap resonance if the barge and the payload are close enough, the cable parameters and so on.

A. Cross product matrix

The skew-symmetric matrix $\mathbf{S}$ of the cross product associated with the vector $\mathbf{u}$ is defined such as:

$$\mathbf{u} \times \mathbf{v} = \mathbf{S}(\mathbf{u})\mathbf{v} \tag{65}$$

The expression of $\mathbf{S}$ for a vector $\mathbf{u} = \begin{pmatrix} u_1 & u_2 & u_3 \end{pmatrix}^T$ is:

$$\mathbf{S}(\mathbf{u}) = \begin{pmatrix} 0 & -u_3 & u_2 \\ u_3 & 0 & -u_1 \\ -u_2 & u_1 & 0 \end{pmatrix} \tag{66}$$

B. Correction for the time derivative of ${}^0\mathbf{V}_0$

From the definition of the linear acceleration, ${}^j\dot{\mathbf{v}}_j = {}^j\mathbf{R}_e \, {}^e\dot{\mathbf{v}}_j$, this term does not match the time-differentiation of ${}^j\mathbf{v}_j = {}^j\mathbf{R}_e \, {}^e\mathbf{v}_j$ because of the projection. A correction is required.

It comes from Rongère and Clément (2013) for the base:

$$\frac{\partial {}^0\mathbf{V}_0}{\partial t} = {}^0\dot{\mathbf{V}}_0 - \begin{pmatrix} \mathbf{S}({}^0\boldsymbol{\omega}_0) \, {}^0\mathbf{v}_0 \\ \mathbf{0}_{3\times 1} \end{pmatrix} \tag{67}$$

References

Babarit, A., Delhommeau, G., 2015. Theoretical and numerical aspects of the open source BEM solver NEMOH, in: Proceedings of the 11th European Wave and Tidal Energy Conference, EWTEC2015.

Bai, W., Hannan, M.A., Ang, K.K., 2014. Numerical simulation of fully nonlinear wave interaction with submerged structures: Fixed or subjected to constrained motion. Journal of Fluids and Structures 49, 534–553. doi:10.1016/j.jfluidstructs.2014.05.011.

Behnel, S., Bradshaw, R., Citro, C., Dalcin, L., Seljebotn, D.S., Smith, K., 2011. Cython: The best of both worlds. Computing in Science and Engineering 13, 31–39. doi:10.1109/MCSE.2010.118.

Cha, J.H., Roh, M.I., Lee, K.Y., 2010. Dynamic response simulation of heavy cargo suspended by a floating crane based on multibody system dynamics. Ocean Engineering 37, 1273–1291. doi:10.1016/j.oceaneng.2010.06.008.

Chauvigné, C., Letournel, L., Babarit, A., Ducrozet, G., Bozonnet, P., Gilloteaux, J.C., Ferrant, P., 2015. Progresses in the development of a weakly-nonlinear wave body interaction model based on the weak-scatterer approximation, in: Proceedings of the ASME 2015 34th International Conference on Ocean, Offshore and Arctic Engineering OMAE2015.

Chin, C., Nayfeh, A.H., Abdel-Rahman, E., 2001. Nonlinear dynamics of a boom crane. Journal of Vibration and Control 7, 199–220. doi:10.1177/107754630100700204.

Combourieu, A., Philippe, M., Rongère, F., Babarit, A., 2014. InWave: a new flexible design tool dedicated to wave energy converters, in: Proceedings of the ASME 2014 33rd International Conference on Ocean, Offshore and Artic Engineering, OMAE2014. doi:10.1115/OMAE2014-24564.

Ellermann, K., Kreuzer, E., 2003. Nonlinear dynamics in the motion of floating cranes. Multibody System Dynamics 9, 377–387. doi:10.1023/A:1023361314261.

Ellermann, K., Kreuzer, E., Markiewicz, M., 2002. Nonlinear dynamics of floating cranes. Nonlinear Dynamics 27, 107–183. doi:10.1023/A:1014256405213.

Elling, R.E., McClinton, A., 1973. Dynamic loading of shipboard cranes, in: IEEE International Conference on Engineering in the Ocean Environment, pp. 174–177. doi:10.1109/OCEANS.1973.1161241.

Featherstone, R., 2008. Rigid body dynamics algorithms. Springer. doi:10.1007/978-1-4899-7560-7.

Felippa, C.A., Park, K.C., Farhat, C., 2001. Partitioned analysis of coupled mechanical systems. Computer Methods in Applied Mechanics and Engineering 190, 3247–3270. doi:10.1016/S0045-7825(00)00391-1.

Gasmi, A., Sprague, M., Jonkman, J., Jones, W., 2013. Numerical stability and accuracy of temporally coupled multi-physics modules in wind-turbine CAE tools, in: Proceedings of the 51st AIAA Aerospace Sciences Meeting including the New Horizons Forum and Aerospace Exposition. doi:10.2514/6.2013-203.

Hall, M., Goupee, A., 2015. Validation of a lumped-mass mooring line model with DeepCwind semisubmersible model test data. Ocean Engineering 104, 590–603. doi:10.1016/j.oceaneng.2015.05.035.

Ham, S.H., Roh, M.I., Lee, H., Ha, S., 2015. Multibody dynamic analysis of a heavy load suspended by a floating crane with constraint-based wire rope. Ocean Engineering 109, 145–160. doi:10.1016/j.oceaneng.2015.08.050.

Hannan, M., Bai, W., 2016. Analysis of nonlinear dynamics of fully submerged payload hanging from offshore crane vessel. Ocean Engineering 128, 132–146. doi:10.1016/j.oceaneng.2016.10.030.

Hannan, M.A., 2014. Numerical simulation of submerged payload coupled with crane barge in waves. Ph.D. thesis. National university of Singapore. doi:10.13140/2.1.4198.2247.

Hourtash, A., 2005. The kinematic hessian and higher derivatives, in: Proceedings of the 2005 IEEE International Symposium on Computational Intelligence in Robotics and Automation. doi:10.1109/CIRA.2005.1554272.

Khalil, W., Chevallereau, C., 1987. An efficient algorithm for the dynamic control of robots in the cartesian space, in: Proceedings of the 26th IEEE Conference on Decision and Control. doi:10.1109/CDC.1987.272906.

Khalil, W., Kleinfinger, J.F., 1986. A new geometric notation for open and closed-loop robots, in: Proceedings of the 1986 IEEE International Conference on Robotics and Automation. doi:10.1109/ROBOT.1986.1087552.

Ku, N., Ha, S., 2014. Dynamic response analysis of heavy load lifting operation in shipyard using multi-cranes. Ocean Engineering 83, 63–75. doi:10.1016/j.oceaneng.2014.03.026.

Ku, N., Roh, M.I., 2015. Dynamic response simulation of an offshore wind turbine suspended by a floating crane. Ships and Offshore Structures 10, 621–634. doi:10.1080/17445302.2014.942504.

Letournel, L., 2015. Développement d'un outil de simulation numérique basé sur l'approche weak-scatterer pour l'étude des systèmes houlomoteurs en grands mouvements. Ph.D. thesis. Ecole Centrale de Nantes.

Letournel, L., Chauvigné, C., Gelly, B., Babarit, A., Ducrozet, G., Ferrant, P., 2018. Weakly nonlinear modeling of submerged wave energy converters. Applied Ocean Research 75, 201–222. doi:10.1016/j.apor.2018.03.014.

Letournel, L., Ducrozet, G., Babarit, A., Ferrant, P., 2017. Proof of the equivalence of Tanizawa-Berkvens' and Cointe-van Daalen's formulations for the time derivative of the velocity potential for non-linear potential flow solvers. Applied Ocean Research 63, 184–199. doi:10.1016/j.apor.2017.01.010.

Li, L., Gao, Z., Moan, T., 2015. Response analysis of a non-stationary lowering operation for an offshore wind turbine monopile substructure. Journal of Offshore Mechanics and Arctic Engineering 137. doi:10.1115/1.4030871.

Malenica, S., Orozco, M., Chen, X.B., 2005. Some aspects of seakeeping of the floating body with attached pendulum, in: Proceedings of the 11th International Congress of the International Maritime Association of the Mediterranean.

Masciola, M., Jonkman, J., Robertson, A., 2014. Extending the capabilities of the mooring analysis program: A survey of dynamic mooring line theories for integration into FAST, in: Proceedings of the ASME 2014 33rd International Conference on Ocean, Offshore and Arctic Engineering, OMAE2014. doi:10.1115/OMAE2014-23508.

Morison, J.R., O'Brien, M.P., Johnson, J.W., Schaaf, S.A., 1950. The force

exerted by surface waves on piles. Petroleum Transactions 189, 149–154. doi:10.2118/950149-G.

Pawlowski, J.S., Bass, D.W., 1991. A theoretical and numerical model of ship motions in heavy seas. SNAME Transactions 99.

Peterson, P., 2009. F2PY: a tool for connecting fortran and python programs. International Journal of Computational Science and Engineering 4, 296–305. doi:10.1504/ijcse.2009.029165.

Piperno, S., Farhat, C., 2001. Partitioned procedures for the transient solution of coupled aeroelastic problems - Part 2: energy transfer analysis and three-dimensional applications. Computer Methods in Applied Mechanics and Engineering 190, 3147–3170. doi:10.1016/S0045-7825(00)00386-8.

Rongère, F., Clément, A.H., 2013. Systematic dynamic modeling and simulation of multibody offshore structures: application to wave energy converters, in: Proceedings of the ASME 2013 32nd International Conference on Ocean, Offshore and Arctic Engineering, OMAE2013.

Schellin, T.E., Jiang, T., Ostergaard, C., 1993. Response analysis and operating limits of crane ships. Journal of Ship Research 37, 225–238.

Schellin, T.E., Jiang, T., Sharma, S.D., 1991. Crane ship response to wave groups. Journal of Offshore Mechanics and Arctic Engineering 113, 211–218. doi:10.1115/1.2919922.

Van Den Boom, H.J.J., Dekker, J.N., Dallinga, R.P., 1988. Computer analysis of heavy lift operations, in: Offshore Technology Conference. doi:10.4043/5819-MS.

Witz, J.A., 1995. Parametric excitation of crane loads in moderate sea states. Ocean Engineering 22, 411–420. doi:10.1016/0029-8018(94)00015-Y.

Wuillaume, P.Y., 2019. Numerical simulation of installation operations for offshore wind farms. Ph.D. thesis. Ecole Centrale de Nantes.

Wuillaume, P.Y., Babarit, A., Rongère, F., Lynch, M., Combourieu, A., Ferrant, P., 2018. Comparison between experiments and a multibody weakly nonlinear potential flow approach for modeling of marine operations, in: Proceedings of the ASME 2018 37th International Conference on Ocean, Offshore and Artic Engineering.

Wuillaume, P.Y., Rongère, F., Babarit, A., Philippe, M., Ferrant, P., 2017. Development and adaptation of the composite rigid body algorithm and the weak-scatterer approach in view of the modeling of marine operations, in: Proceedings of the 23ème Congrès Français de Mécanique, CFM2017.